J. Fluid Mech. (1995), *vol.* 298, *pp.* 167–192

A spectral boundary element approach to three-dimensional Stokes flow

By G. P. MULDOWNEY† AND J. J. L. HIGDON
Department of Chemical Engineering, University of Illinois, Urbana, IL 61801, USA

(Received 14 September 1994 and in revised form 6 April 1995)

A novel method is introduced for solving the three-dimensional Stokes equations via a spectral element approach to the boundary integral method. The accuracy and convergence of the method are illustrated through applications involving rigid particles, deformable droplets and interacting particles. New physical results are obtained for two applications in low Reynolds number flow: the permeability of periodic models of a porous membrane and the instability of a toroidal droplet subject to non-axisymmetric perturbations. Further applications are described in the companion paper (Higdon & Muldowney 1995).

1. Introduction

Over the past two decades, the boundary integral method has proven to be a versatile technique for the solution of the Stokes equations for low Reynolds flow. The application of this technique to the three-dimensional Stokes equations was first introduced by Youngren & Acrivos (1975) for flow past rigid particles. The method was quickly adopted for flow past deformable drops and bubbles (Youngren & Acrivos 1976) and has since been used in numerous studies involving droplet deformation and breakup (see e.g. Rallison 1984; Pozrikidis 1992; Stone 1994). Beyond these initial applications, the boundary integral method has been employed to study microscopic flow in porous media (Zick & Homsy 1982; Larson & Higdon 1986, 1987), particle–wall interactions (see Weinbaum *et al.* 1990), flow over cavities (Higdon 1985, 1990), the swimming of microscopic organisms (Phan-Thien, Tran-Cong & Ramia 1987), the deformation of red blood cells (Li Barthes-Biesel & Helmy 1988; Pozrikidis 1990) and the design of experiment devices (Higdon 1993). The boundary integral method has also been proposed as an alternative to multipole expansion methods for the simulation of many-body problems in concentrated suspensions (Kim & Karrila 1991). These references illustrate the breadth and diversity of boundary integral methods in low Reynolds number flow, yet they represent only a small sample of the boundary integral applications appearing in the fluid dynamics literature. Additional references and background material may be found in the review articles cited above and in the recent monographs by Kim & Karrila (1991) and Pozrikidis (1992).

Many versions of the boundary integral method for Stokes equations have been developed with different strategies for the *formulation* of the integral equations and the *discretization* of the boundary variables. In the formulation, different approaches lead to Fredholm integral equations of the first kind, of the second kind or of mixed type. In the discretization of the integral equation, the boundary may be treated as a single domain, or divided into a number of subdomains with a suitable discretization defined

† Present address: Mobil Research and Development Co, Billingsport Rd, Paulsboro, NJ 08066, USA.

on each region. Early implementations of the boundary integral method (e.g. Youngren & Acrivos 1975) employed a zeroth-order discretization with the boundary divided into a large number of planar surface elements and the physical variables, surface stress and velocity, defined as constants over each surface element. At the other extreme, a boundary integral method may employ a single domain with the physical variables represented as high-order orthogonal expansions such as spherical harmonics (see e.g. Zick & Homsy 1982). This approach yields high accuracy with a minimum number of unknowns; however, it is limited to idealized geometries such as spheres and rectangular domains.

To achieve increased accuracy while maintaining versatility, one may divide the boundary into a collection of surface elements with first-order, second-order or higher discretizations on each element. This approach has been implemented for both two-dimensional (Higdon 1985) and three-dimensional Stokes flows (Schnepper 1988; Higdon & Schnepper 1994). Alternative discretizations based on finite element methods have also been developed with both linear and quadratic elements (Chan, Beris & Advani 1992).

A significant development in finite element methodology has been the *spectral element method* in which high-order bases are defined in terms of orthogonal polynomials (Maday & Patera 1989). The attraction of this approach is that it exploits the exponential convergence associated with spectral methods while retaining the versatility of the finite element method. The disadvantage of spectral element methods compared with low-order finite element methods is that the spectral basis increases the bandwidth of the sparse system matrices, increasing the computational effort. Thus the increased accuracy of the spectral representation must be balanced against the increased computational cost.

The spectral element approach may be exploited in a boundary integral formulation by utilizing *spectral boundary elements*. In the boundary integral method, the linear systems arising from the discretized integral equation involve dense system matrices independent of the form of discretization. Thus the solution of the linear system for a spectral boundary element method requires no more effort than that for a low-order boundary integral method with the same number of unknowns. One achieves all of the benefits of spectral discretizations without incurring any additional computational cost. High-order polynomial bases have been used by numerous authors (Guo, von Petersdorff & Stephan 1990; Parriera 1988; Rank 1988; Alarcon & Reverter 1986) for two-dimensional boundary integral application in potential flow, elastostatics and other applications. In our own studies, (Occhialini, Muldowney & Higdon 1992; Occhialini & Higdon 1992; Higdon 1993), we have employed the spectral boundary element method for two-dimensional Stokes flows in a variety of geometries with excellent results.

To this date, there has been no application of the spectral boundary element method to three-dimensional Stokes flow. In fact, the authors are not aware of any study incorporating a true spectral boundary element approach for three-dimensional domains. Cerrolaza & Alarcon (1987) discussed the use of Legendre polynomials as an adaptive basis for three-dimensional potential problems and presented limited results for simple geometries. However, the addition of higher-order basis functions in an adaptive sense does not realize the potential of a spectral formulation. Specifically, such a method does not yield the exponential convergence of spectral expansions, nor does it exploit the computational efficiencies of tensor product bases. (See Canuto *et al.* 1988.)

The goal of the present effort is to develop a robust spectral boundary element

algorithm for three-dimensional Stokes flows. In pursuing this goal, we pay particular attention to the practical problems which are encountered in applying the algorithm to physical problems of interest to fluid dynamicists. In the following sections, we discuss (i) the formulation and discretization of the integral equations, (ii) the development of effective strategies for numerical integration, (iii) convergence results for numerical test cases, and (iv) the use of these algorithms in typical applications in low Reynolds number flow. In a companion paper (Higdon & Muldowney 1995), we employ the spectral boundary element method to compute the resistance functions for spherical particles, droplets and bubbles in cylindrical domains.

2. Boundary integral formulation

The governing equations for low Reynolds number flow are the Stokes equations

$$\nabla\cdot\boldsymbol{\sigma} \equiv -\nabla p+\mu\nabla^2\boldsymbol{u} = 0 \tag{1}$$

and the continuity equation

$$\nabla\cdot\boldsymbol{u} = 0. \tag{2}$$

Following Oseen (see Happel & Brenner 1973, pp. 79–81), one may introduce the fundamental solution $\boldsymbol{S}$ and its associated stress $\boldsymbol{T}$:

$$S_{ik}(\hat{\boldsymbol{x}}) = \frac{\delta_{ik}}{r}+\frac{\hat{x}_i\hat{x}_k}{r^3}, \tag{3}$$

$$T_{ijk}(\hat{\boldsymbol{x}}) = -6\frac{\hat{x}_i\hat{x}_j\hat{x}_k}{r^5}, \tag{4}$$

where $\hat{\boldsymbol{x}} = \boldsymbol{x}-\boldsymbol{x}_0$ and $r = |\hat{\boldsymbol{x}}|$.

With these expressions, the velocity at a point $\boldsymbol{x}_0$ on the boundary of the fluid domain S_B may be expressed in the integral form (Pozrikidis 1992; Higdon & Schnepper 1994)

$$u_k(\boldsymbol{x}_0) = -\frac{1}{4\pi\mu}\int_{S_B}(S_{ik}f_i(\boldsymbol{x})-\mu T_{ijk}\,u_i(\boldsymbol{x})\,n_j)\,\mathrm{d}S, \tag{5}$$

where $\boldsymbol{f} = \boldsymbol{\sigma}\cdot\boldsymbol{n}$ is the surface stress and the normal vector $\boldsymbol{n}$ points into the fluid.

For boundary value problems with velocity boundary conditions, the integral formula (5) leads to Fredholm integral equations of the first kind. First-kind equations may lead to ill-conditioned systems, and there is some concern over the use of these equations for robust numerical computations. Hsiao (1988) conducted a rigorous stability analysis for the solution of first-kind integral equations for the two-dimensional Laplace's equation. He showed that smooth convergence may be achieved and discussed the limits of resolution imposed by high condition numbers and round-off error. In our own work, we have found that spectral boundary element algorithms based on first-kind equations are quite robust and yields results of extremely high precision.

To avoid the problems associated with first-kind equations, a number of authors (Hebeker 1986, 1988; Power & Miranda 1987; Kim & Karrila 1991; Pozrikidis 1992; Ingber & Mondy 1993) have suggested formulations based on equations of the second kind. Ingber & Mondy develop a second-kind equation for the surface stress based on the integral formula:

$$f_k(\boldsymbol{x}_0) = \frac{1}{4\pi}\int_{S_B}[T_{ikl}\,n_l(\boldsymbol{x}_0)f_i(\boldsymbol{x})-\mu Q_{ijkl}\,n_j\,n_l(\boldsymbol{x}_0)\,(u_i(\boldsymbol{x})-u_i(\boldsymbol{x}_0))]\,\mathrm{d}S \tag{6}$$

where

$$Q_{ijkl}(\hat{x}) = \left(4\frac{\delta_{ij}\delta_{kl}}{r^3} + 6\frac{\delta_{ik}\hat{x}_j\hat{x}_l + \delta_{il}\hat{x}_j\hat{x}_k + \delta_{jk}\hat{x}_i\hat{x}_l + \delta_{jl}\hat{x}_i\hat{x}_k}{r^5} - 60\frac{\hat{x}_i\hat{x}_j\hat{x}_k\hat{x}_l}{r^7}\right). \quad (7)$$

For viscous free surface flows, neither the velocity nor the surface stress are known explicitly; however, both must satisfy continuity conditions across the fluid interface. In these circumstances, we write an integral formula (5) for each fluid region and subtract the results to obtain an equation for the surface velocity in terms of the jump in surface stress. Let a body of fluid with density ρ_1 and viscosity $\lambda\mu$ be immersed in an infinite fluid with density ρ_2 and viscosity μ.

The integral for $\boldsymbol{u}$ may be expressed as

$$u_k(\boldsymbol{x}_0) - \frac{2}{1+\lambda}u_k^{\infty}(\boldsymbol{x}_0) = -\frac{1}{1+\lambda}\frac{1}{4\pi\mu}\int_{S_B}(S_{ik}\,\Delta f_i(\boldsymbol{x}))\,\mathrm{d}S + \frac{1-\lambda}{1+\lambda}\frac{1}{4\pi}\int_{S_B}(T_{ijk}\,u_i(\boldsymbol{x})\,n_j)\,\mathrm{d}S. \quad (8)$$

(See Pozrikidis 1992 or Higdon & Schnepper 1994 for details.)

With constant surface tension γ and gravitational acceleration $\boldsymbol{g}$, the jump in surface stress $\Delta\boldsymbol{f}$ is given by

$$\Delta\boldsymbol{f} = \gamma(\nabla\cdot\boldsymbol{n})\,\boldsymbol{n} + (\rho_2 - \rho_1)(\boldsymbol{g}\cdot\boldsymbol{x})\,\boldsymbol{n}. \quad (9)$$

The integral formulae (5), (6) and (8) provide the basis for the integral equations most commonly encountered in three-dimensional Stokes flow. In the following sections, we consider optimal strategies for the discretization, integration and solution of these equations.

3. Spectral boundary element discretization

Let the boundary surface of a three-dimensional body be divided into a collection of curvilinear quadrilateral surface elements S_α, $\alpha = 1, N_E$. (See figure 1.) On each surface element, define a two-dimensional parametric representation with variables ξ and η on the interval $[-1, 1]$. On each surface element, define *geometry collocation points* $\boldsymbol{x}(\xi_i, \eta_j)$, $i = 1, N_G$, $j = 1, N_G$, where the values of (ξ_i, η_j) are chosen as the zeros of the N_Gth-order polynomial from a family of orthogonal polynomials. In general, both Chebyshev and Legendre polynomials yield excellent results in approximating smooth functions (Gottlieb & Orszag 1984), and we have employed both with comparable results. In some circumstances, there is a slight advantage to using Legendre polynomials, because the points correspond to the evaluation points for a Gauss–Legendre quadrature formula. All work described in this paper is based on the use of Legendre polynomials.

With the collocation points specified, the position of any point along the surface is expressed as a Lagrangian interpolant with respect to ξ and η; that is

$$\boldsymbol{x}(\xi,\eta) = \sum_{i=1}^{N_G}\sum_{j=1}^{N_G}\boldsymbol{x}(\xi_i,\eta_j)\,h_i(\xi)\,h_j(\eta), \quad (10)$$

where h_i is the (N_G-1)-order Lagrangian interpolant polynomial defined by $h_i(\xi_j) = \delta_{ij}$.

All geometrical quantities such as tangent vectors, normal vectors, surface curvature,

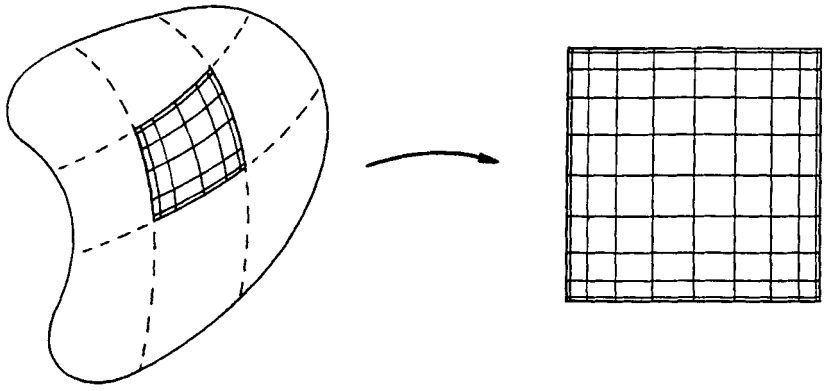

FIGURE 1. Mapping of spectral boundary element to square $[-1, 1]\times[-1, 1]$.

etc. may be calculated as derivatives of the geometry interpolating functions. Because the polynomial representation is of high order, analytical differentiation yields derivative quantities without significant loss of accuracy. It proves convenient to define a differentiation matrix

$$d_{ki} \equiv h_i'(\xi_k) \tag{11}$$

and thus to express derivatives in the compact forms

$$\boldsymbol{x}_{\xi_{kl}} = d_{ki}\,\boldsymbol{x}_{il}, \quad \boldsymbol{x}_{\eta_{kl}} = d_{lj}\,\boldsymbol{x}_{kj}, \tag{12}$$

where the summation convention is assumed in (12).

In the literature on spectral methods, the differentiation matrix d_{ki} is referred to as the collocation derivative. The definition (11) is valid for any choice of collocation points and may be evaluated directly from the general expression for a Lagrangian interpolant. For special choices of ξ_i such as Legendre or Chebyshev collocation points, closed-form expressions for d_{ki} are available. (See Canuto *et al.* 1988, §§2.3, 2.4). For the efficient evaluation of derivatives at an arbitrary collection of points, it proves effective to evaluate the derivatives at the collocation points using (12) and to interpolate to the desired points using an equation analogous to (10).

With the specification of the boundary geometry completed, we turn to the representation of the physical variables $\boldsymbol{u}$ and $\boldsymbol{f}$. We define a set of *basis collocation points* $\boldsymbol{x}(\xi_i, \eta_j)$, $i = 1, N_B$, $j = 1, N_B$, where the values of (ξ_i, η_j) are chosen as before, i.e. as the zeros of an (N_B-1)-order Legendre polynomial. All physical variables $\boldsymbol{u}$ and $\boldsymbol{f}$ are then defined as interpolants of the form

$$\boldsymbol{u}(\xi, \eta) = \sum_{i=1}^{N_B}\sum_{j=1}^{N_B} \boldsymbol{u}(\xi_i, \eta_j)\, h_i(\xi)\, h_j(\eta), \tag{13}$$

where h_i is the (N_B-1)-order Lagrangian interpolant polynomial defined by $h_i(\xi_j) = \delta_{ij}$.

In defining the discrete representations above, we emphasize that a Lagrangian interpolant through the specified collocation points is exactly equivalent to an expansion in terms of the associated orthogonal polynomials. Specifically, if one computes the coefficients of a Legendre polynomial expansion employing Gauss–Legendre quadrature, the N_B-term truncated series is identical to the N_B-point Lagrangian interpolant through these N_B quadrature points. Given this equivalence, the accuracy and convergence properties of the spectral element discretization may be inferred from those of the orthogonal polynomial series. For smooth functions with

continuous derivatives of all orders, a finite series has a truncation error proportional to e^{-cN_B} (see Gottlieb & Orszag 1984; Canuto *et al.* 1988). This exponential convergence is the basis for the remarkable accuracy of spectral element methods. The enhanced convergence compared to low-order methods is analogous to that observed in comparing Gaussian quadrature formulae with Simpson's or trapezoid rules. In addition to the favourable convergence rate, interpolants based on orthogonal polynomials have excellent properties with respect to numerical stability. By contrast, it is well known (Gottlieb & Orszag 1984; Isaacson & Keller, 1966, §3.4) that high-order interpolants based on equally spaced points are subject to severe round-off error and numerical instability.

With the discretization of the physical and geometry variables set, we substitute into the boundary integral formula (5), or its equivalent, and require that the integral equation be satisfied at the discrete set of basis collocation points $\boldsymbol{x}(\xi_i, \eta_j)$, $i = 1, N_B$, $j = 1, N_B$. The discrete form of the integral equation yields a linear system of three $N_E N_B^2$ algebraic equations:

$$\boldsymbol{u} = \boldsymbol{A}\boldsymbol{f} + \boldsymbol{B}\boldsymbol{u}. \tag{14}$$

These equations, combined with the boundary data at the $N_E N_B^2$ basis points yields a consistent set of three $N_E N_B^2$ equations in three $N_E N_B^2$ unknowns.

The matrices $\boldsymbol{A}$ and $\boldsymbol{B}$ in the discrete system are defined as integrals of the kernels and basis functions over the collection of surface elements. Each matrix is composed of elemental submatrices $\boldsymbol{A}^{\alpha\beta}$, $\boldsymbol{B}^{\alpha\beta}$ giving the velocity at points on element α due to integrals over element β. The submatrices are defined in the form

$$\left.\begin{aligned} \boldsymbol{A}^{\alpha\beta}(k,l;m,n) &= -\frac{1}{4\pi\mu}\int_{-1}^{1}\int_{-1}^{1} \boldsymbol{S}(\boldsymbol{x}^{\beta}(m,n)-\boldsymbol{x}^{\alpha}(k,l))\, h_m(\xi)\, h_n(\eta)\, \omega \,\mathrm{d}\xi\,\mathrm{d}\eta, \\ \boldsymbol{B}^{\alpha\beta}(k,l;m,n) &= \frac{1}{4\pi}\int_{-1}^{1}\int_{-1}^{1} \boldsymbol{T}(\boldsymbol{x}^{\beta}(m,n)-\boldsymbol{x}^{\alpha}(k,l))\, h_m(\xi)\, h_n(\eta)\, \omega \,\mathrm{d}\xi\,\mathrm{d}\eta, \end{aligned}\right\} \tag{15}$$

where ω is the differential area element defined by $\mathrm{d}S = \omega\,\mathrm{d}\xi\,\mathrm{d}\eta$.

The accurate and efficient evaluation of these elemental integrals is critical to the success of the spectral boundary element method.

4. Numerical integration on spectral boundary elements

Owing to its high-order discretization, the spectral boundary element method requires special attention with respect to efficient numerical quadrature algorithms. In low-order boundary element methods, the boundary surfaces are divided into a large number of surface elements of small size and simple shape. On each element, one must integrate a singular kernel multiplied by a small number of basis functions. Under these conditions, simple transformations (Duffy 1982) and multi-level domain subdivision (Chan *et al.* 1992) may be employed for accurate quadratures. By contrast, spectral boundary elements may cover a large surface area with complex shapes and high curvature. Integrations are required on a much smaller number of elements, but with a much larger number of basis functions. Under these conditions, it is more efficient to employ a single high-order quadrature algorithm over the entire element. If the algorithm is based on a product of one-dimensional rules $[\xi_i \times \eta_j]$, the operation count for interpolation and function evaluation is further reduced. (This is a characteristic feature of all product bases in spectral methods.) In the discussion below, we consider two separate quadrature problems: (i) singular integrals when the collocation point

falls on the element of integration and (ii) nearly singular integrals where the collocation points lies close to the element, but the kernel is non-singular.

4.1. *Singular quadratures*

Consider a spectral element with variables (ξ, η) defined on the interval $[-1, 1]$. Let a collocation point be located at position (ξ_0, η_0) and define variables $\hat{\xi} = \xi - \xi_0$, $\hat{\eta} = \eta - \eta_0$. The kernels of the integral formulae (5) etc., have r^{-1} singularities at the collocation point. (The $\boldsymbol{T}$ kernel appears to be more singular; however, $\hat{\boldsymbol{x}} \cdot \boldsymbol{n}$ is $O(r^2)$ for small r yielding an r^{-1} singularity.) With the polynomial bases for $\boldsymbol{f}$ and $\boldsymbol{u}$ and the geometry mapping for $\hat{\boldsymbol{x}}$, the singular integrals are of the form

$$I = \int_{-1}^{1} \int_{-1}^{1} \frac{g(\xi, \eta)\, \mathrm{d}\xi\, \mathrm{d}\eta}{(a\hat{\xi}^2 + 2b\hat{\xi}\hat{\eta} + c\hat{\eta}^2 + O(\hat{\xi}^m \hat{\eta}^{3-m}))^{1/2}}. \tag{16}$$

The most efficient procedure we have found for integrals of this type is based on variable mappings which cluster quadrature points close to the position of the singularity. For simplicity, consider the case with (ξ_0, η_0) at the origin and examine the integral on the first quadrant $\xi > 0$, $\eta > 0$. Let z_i and z_j denote standard Gauss–Legendre quadrature points and let s_i and t_j denote the shifted points $s_i = \frac{1}{2}(1 + z_i)$ and $t_j = \frac{1}{2}(1 + z_j)$. Define mapped variables

$$\xi_i = \left(\frac{\sinh \beta s_i}{\sinh \beta}\right)^2, \quad \eta_j = \left(\frac{\sinh \beta t_j}{\sinh \beta}\right)^2, \tag{17}$$

where β is an empirical parameter with a value $\beta = 4$ yielding the best overall performance.

The mapping clusters points near the singularity while maintaining a regular spacing over the remainder of the interval. It is a product mapping which maintains the tensor product efficiency discussed above. We have conducted extensive tests of this quadrature algorithm for integrals of the form (16) with the $O(\hat{\xi}^m \hat{\eta}^{3-m})$ term set to zero. These tests show exponential convergence in all cases.† The integrations with non-zero cubic terms perform similarly, because the simple stretching transformation is insensitive to the exact type of singularity. Quadrature counts for these integrations are larger than those for simple elements, however, these integrations cover a large spectral element with many nodes. A spectral element with a basis $N_B = 12$ has 144 total nodes. With a 24×24 quadrature of each of 4 quadrants, the total number of quadrature points/node is equivalent to a 4×4 point quadrature on each element for a zeroth order method with an equal number of nodes. The computational effort in each integration is dominated by the evaluation of the geometry and kernel functions. All N_B basis evaluations require only a modest effort owing to the tensor product basis. Moreover, these evaluations are expressed as matrix multiplications which may be evaluated with machine coded BLAS3 calls.

4.2. *Non-singular quadratures*

Non-singular quadratures arise when integrating over a given element with a collocation point located on a different element. If the collocation point lies far from the given element, a straightforward product Gaussian quadrature is effective. On the other hand, if the collocation point lies in close proximity to the element, the nearly singular kernel will yield poor convergence.

† Detailed tabulations for all quadrature tests described in this section are available from the editorial office, or directly from the author.

Our development for nearly singular integrals is based on quadrature techniques for one dimensional integrals of the form

$$I = \int_{-1}^{1} \frac{g(\xi)\,d\xi}{((\xi-\xi_0)^2+h^2)^{m/2}}. \tag{18}$$

The nearest singularities in the complex plane are located at $\xi = \xi_0 \pm ih$, and ideally we wish to map these points to infinity, e.g. $s = \hat{\xi}/(\hat{\xi}^2+h^2)^{1/2}$. Unfortunately, mappings of this type bring the point at infinity into a finite distance, e.g. to $s = \pm 1$, and introduce singularities associated with the polynomial in the numerator. Instead, we seek mappings which move the point of singularity away from the interval of integration, while leaving the point at infinity at a respectful distance. After testing numerous strategies, we have found the best choice to be mappings of the form

$$\xi = \xi_0 + h \sinh(n \sinh^{-1} s) \tag{19}$$

which expresses ξ as an algebraic function of s. The optimal choice for the integer n is the greatest integer $< (1+\ln \epsilon^{-1})$ where ϵ is based on the minimum distance of the singularity from the interval, specifically

$$\epsilon = h \quad \text{if} \quad |\xi_0| < 1, \quad \epsilon = \min\{h, |\xi_0|-1\} \quad \text{if} \quad |\xi_0| > 1. \tag{20}$$

With the mapping (19), the variable ξ is replaced by s, and the integration with respect to s is performed with standard Gauss–Legendre quadrature. If ξ_0 lies within the interval $[-1, 1]$, the interval is split with separate quadratures on each subinterval. If a collocation point is located far from the interval, (20) yields $n = 1$, and the transformation (19) reduces to a linear transformation, i.e. standard Gauss–Legendre quadrature.

Numerical tests of this algorithm demonstrate exponential convergence for all values of h, with smaller h requiring higher quadrature counts for the same accuracy. Comprehensive tests of this algorithm have been conducted for a range of h and ξ_0, and we have developed a simple estimate for the number of quadrature points required as a function of ϵ defined above:

$$N_Q = N_0 + 8 \log_{10}(\epsilon^{-1}). \tag{21}$$

If N_0 yields a given accuracy for $\epsilon = 1$, then N_Q points will guarantee the same accuracy independent of ϵ. While the coefficient in this relationship is empirical, its functional form may be inferred from the variable mapping (19).

With a well-defined procedure for one dimensional nearly singular integrals, we consider two-dimensional integrals of the type encountered in the spectral boundary element algorithm,

$$I = \int_{-1}^{1}\int_{-1}^{1} \frac{g(\xi,\eta)\,d\xi\,d\eta}{(a\hat{\xi}^2+2b\hat{\xi}\hat{\eta}+c\hat{\eta}^2+f)^{1/2}}. \tag{22}$$

Integrals of this form are evaluated by the use of a product rule based on the one-dimensional quadratures described above. For each variable ξ and η, one determines ξ_0 and η_0 corresponding to the minimum value of h as expressed in integrals of the form (18). This choice determines the location of the independent quadrature points ξ_i and η_j for the two-dimensional integration. Numerical tests show excellent performance for this product integration rule. The success of this strategy is based on the smooth mapping properties of (19) which move the nearest singularities away from the domain of integration.

The quadrature methods for singular and nearly singular integrals described above were developed with special attention to the requirements of the spectral element

discretization. Prior to the development of these algorithms, we made an extensive study of the boundary integral and numerical integration literature (Hammerlin 1979, 1982; Braß & Hammerlin 1982; Espelid & Genz 1992). We tested analytical quadratures, triangle and polar mappings, Gaussian routines with specialized weights (e.g. $w(x) = (ax^2+bx+c)^{-1/2}$), product integration algorithms, and an assortment of analytical techniques. We have performed analytical integrations for asymptotic approximations of the integrand, extracting terms up to seventh order in $(\hat{\xi}, \hat{\eta})$, combined with numerical quadratures for the remainder. Each of these approaches proved less efficient than the procedures described above. This result may be attributed to two points made by Lyness (1992): (i) a method which is very good for one dimensional quadratures, or two-dimensional squares may not work for an element subject to even a linear mapping, (ii) an algorithm which is exact for a certain type of singularity may be very poor for a different singularity even if they are in some sense 'very close'. On the other hand, methods which map the singularity away from the domain of integration are insensitive to its exact form and perform well for non-simple geometries. A number of techniques similar to those proposed here are described by Hayami (1992), however those algorithms are not as efficient as the (ξ, η) product rules for spectral element discretization.

5. Numerical results

In the previous sections, we have given a detailed description of the formulation, discretization and integration steps involved in the spectral boundary element method. Here, we present a series of numerical examples which illustrate the performance of this method. For the first test case, we consider rigid oblate spheroidal particles with uniform flow U parallel to the minor axis of the particle. Boundary elements are defined by projecting from the surface of the spheroid to the faces of a rectangular prism of the same aspect ratio. In the first discretization, six elements are employed with a single element on each face of the prism. In the second, the lateral faces of the prism are bisected at the equator yielding a ten-element discretization.

The results in table 1(*a*) show the convergence of the force with increasing order of the spectral basis N_B using an isoparametric discretization with $N_G = N_B$. The results in the first column show the exponential convergence for a spheroid of aspect ratio 4:1 with an error of order 1×10^{-5} at $N_B = 12$. By contrast, the results for the 10:1 aspect ratio yield an error of 1.5×10^{-3} for the same order basis. For large aspect ratios such as 10:1, the surface stress changes very rapidly around the equator of the particle, and the 12th-order basis lacks sufficient resolution in this region. While one could achieve higher resolution with higher-order bases, that is not the most effective strategy. The collocation points associated with orthogonal polynomials cluster near the edges of the elements and away from the centre. In the six-element layout on the spheroid, the equator falls in the centre of an element yielding a less than optimal discretization. To correct this deficiency, the ten-element layout bisects each of the lateral faces of the prism, placing the equator at the edge of an element. Now, the collocation points cluster near the region of greatest change. Columns 3 and 4 demonstrate the effectiveness of this approach with an error of order 1×10^{-7} for $N_B = 7$ in the 4:1 case, and $N_B = 11$ in the 10:1 case. Even in the extreme case of a 100:1 spheroid (column 5) the force has converged to an error of 1.6×10^{-4}. All results in table 1(*a*) employ quadrature counts of $N_Q = 25$ for the singular integrals and $N_0 = 15$ points for the non-singular cases. Smaller quadrature counts may be employed in cases where one does not require seven-figure accuracy in the calculated forces.

(a) N_B	Six elements 4:1	Six elements 10:1	Ten elements 4:1	Ten elements 10:1	Ten elements 100:1
4	0.0066255	0.0299629	0.0000793	−0.0007954	−0.0012846
5	−0.0034503	−0.0341150	0.0000067	−0.0000023	−0.0013646
6	0.0010737	0.0125938	−0.0000007	0.0000470	−0.0014931
7	−0.0005993	−0.0132420	−0.0000001	0.0000122	−0.0012777
8	0.0002086	0.0058063	0.0000000	−0.0000011	−0.0010288
9	−0.0001180	−0.0056851	−0.0000001	−0.0000017	−0.0007550
10	0.0000441	0.0028841	−0.0000001	−0.0000006	−0.0005122
11	−0.0000239	−0.0025469	−0.0000001	−0.0000001	−0.0003120
12	0.0000103	0.0015548	−0.0000001	0.0000000	−0.0001634
Exact	0.8673470	0.8524506	0.8673470	0.8524506	0.8488681

(b) N_B	# nodes	Chan *et al.*	$N_E = 4$ 1st kind	$N_E = 4$ 2nd kind	$N_E = 4$ 2nd kind	$N_E = 10$ 1st kind
3	36	—	0.0209888	0.0251892	0.0281233	—
—	48	−0.03511	—	—	—	—
4	64	—	−0.0102351	−0.0991939	−0.0877546	—
3	90	—	—	—	—	−0.0059831
5	100	—	−0.0044392	−0.0919945	−0.1338171	—
—	120	−0.00835	—	—	—	—
6	144	—	−0.0013367	0.0105932	0.0194136	—
4	160	—	—	—	—	−0.0007954
7	196	—	−0.0001422	0.0007348	−0.0018926	—
—	224	−0.00099	—	—	—	—
5	250	—	—	—	—	−0.0000023
8	256	—	0.0000668	−0.0010180	−0.0013333	—
9	324	—	0.0000595	−0.0000242	−0.0000179	—
6	360	—	—	—	—	0.0000470
10	400	—	0.0000217	−0.0003609	−0.0004268	—
11	484	—	0.0000047	−0.0000461	−0.0000562	—
7	490	—	—	—	—	0.0000122
12	576	—	−0.0000023	0.0000424	0.0000478	—
8	640	—	—	—	—	−0.0000011
13	676	—	−0.0000028	0.0000441	0.0000516	—
14	784	—	−0.0000016	0.0000200	0.0000220	—
9	810	—	—	—	—	−0.0000017
10	1000	—	—	—	—	−0.0000006
11	1210	—	—	—	—	−0.0000001
12	1440	—	—	—	—	0.0000000

TABLE 1(*a*). Dimensionless force $F/(6\pi\mu aU)$ for oblate spheroids in a uniform flow U parallel to the minor axis of particle for aspect ratios 4:1, 10:1 and 100:1. Columns show the convergence of the spectral element computation as a function of increasing order of basis N_B. Discretization employs 6 or 10 elements as described in text. (*b*) Error in dimensionless force $F/(6\pi\mu aU)$ for 10:1 oblate spheroids in a uniform flow U parallel to the minor axis. The exact force is 0.8524506. Columns show the error on using different implementations of the boundary element method. Column 3, computations of Chan *et al.* (1992); column 4, four spectral elements with integral equation of first kind (5); column 5, same discretization as column 4, but integral equation of second kind (6) with velocity constraints; column 6 same as column 5, but with force constraints; column 7, ten spectral elements with integral equation of first kind (6). Entries are listed in order of total number of nodes.

All computations were performed on IBM RS6000/320 workstations or SGI Challenge multiprocessor computers. The computation time required for the boundary integral calculation may be divided into two parts: t_{SETUP} the time required to perform the numerical integrations and to setup the system matrices; and t_{SOLVE}, the time required to solve the linear system of equations. For six-element computations on a single SGI Challenge node, typical c.p.u. times ranged from $t_{SETUP} = 6$ s, $t_{SOLVE} = 0.5$ s for $N_B = 4$, to $t_{SETUP} = 39$ s, $t_{SOLVE} = 24$ s for $N_B = 8$, *to* $t_{SETUP} = 166$ s, $t_{SOLVE} = 255$ s for $N_B = 12$. The number of linear equations in these three examples was 288, 1152 and 2592 respectively. These time estimates are based on a straightforward computation with no utilization of symmetry in the solution. In fact, many problems include one or more planes of symmetry which drastically reduce the computational effort. In the example above, even an arbitrary ellipsoid with distinct lengths for each axis contains three symmetry planes. Exploiting this symmetry reduces t_{SETUP} by a factor of 8 and t_{SOLVE} by a factor of 8^3. In addition, memory requirements are reduced by a factor of 8^2. Thus the numbers for a general ellipsoid with a six-element, $N_B = 12$ computation reduce to $t_{SETUP} = 21$ s, $t_{SOLVE} = 0.5$ s. Multiprocessor runs on the SGI Challenge showed a nearly linear decrease in c.p.u. time up to eight processors, with some fall off for more processors owing to saturation of the shared memory bus. Computation times on the IBM RS6000/320 were approximately 2.4 times those on a single SGI node.

In our next test, we focus on the case of the 10:1 oblate spheroid and consider different strategies for the formulation and discretization of the integral equations. We include the second-order results of Chan *et al.* (1992), the ten-element results from above, as well as spectral element results for four elements using both first- and second-kind formulations. The four-element spectral discretization divides a sphere into four quadrants and maps the spherical coordinates θ and ϕ onto the spheroid. The results in table 1(*b*) are tabulated in order of the total number of nodes with the order of the spectral basis included in each case.

Spectral element methods generally provide the best approach when extremely high precision is required; however, low-order methods often prove favourable when low accuracy is tolerable. In the present case, we find that the spectral discretization is quite competitive even at modest standards of accuracy. For each of the computations reported by Chan *et al.* the spectral element computations yield a smaller error with fewer nodes. With a 1% error tolerance, both spectral discretizations out perform the second-order method, with the four-element, 100-node spectral element error roughly half that of the 60-element, 120-node computation of Chan *et al.* At a tolerance of 0.1%, the 196-node spectral calculation yields an error seven times smaller than the 224-node low-order method. Our conclusion is that the spectral boundary element discretization is at least competitive with low-order methods at any precision and will provide superior performance as precision requirements increase. Note that these spectral element computations employed the same basis N_B on all elements and in each variable ξ, η. Further increases in efficiency might be realized through an optimized choice of bases on different elements.

The second issue to be addressed from table 1(*b*) is the relative performance of the first-kind (5) and second-kind (6) integral formulations using the identical four-element discretization. For the second-kind formulation, additional equations are required to constrain the six rigid body eigensolutions. Two techniques were employed with comparable results. In the first, the first-kind equation (5) was integrated over the surface to supply velocity constraints, while in the second, the total force on the particle was specified, and the normalized resistance computed from the resulting velocity.

	Four elements	Ten elements	
N_B	4:1	4:1	10:1
4	0.192178	0.027036	0.124459
5	0.052882	0.006342	0.056897
6	0.012879	0.002101	0.026161
7	0.006526	0.000980	0.011362
8	0.003839	0.000449	0.006465
9	0.002133	0.000182	0.003997
10	0.001060	0.000070	0.002090
11	0.000401	0.000023	0.000799
Exact	0.48772	0.48772	0.3294

TABLE 2. Error in surface velocity on oblate spheroidal droplet (aspect ration 4:1, 10:1) with viscosity ratio $\lambda = 2$ immersed in an extensional flow (23) with strain rate e and capillary number $\mu ea/\gamma = 1$. Columns show maximum error in velocity $|\boldsymbol{u} - \boldsymbol{u}_{EXACT}|/ea$. Maximum error in each case occurs at the equator. The last value in each column gives the radial velocity at this point evaluated with $N_B = 12$; these values are accurate to the number of figures shown.

Both integral formulations yield exponential convergence in the overall force; however, the first-kind formulation yields consistently smaller errors. The superior performance of the first-kind formulation is consistent with the findings of Ingber & Mondy (1993) using low-order boundary elements. While first-kind formulations may yield better overall accuracy, second-kind formulations may prove useful in applications where iterative solutions are utilized. See Kim & Karilla (1991) for further discussion of this issue.

The results presented in table 1 demonstrate the robustness of the spectral boundary element method for flows with rigid boundaries. In our next example, we investigate the performance for free surface flows, using the integral equation of the second kind (8) for the surface velocity of a liquid droplet in a three-dimensional flow field.

We consider an oblate spheroidal droplet with minor axis parallel to the z-axis subject to an extensional flow with characteristic strain rate e:

$$\boldsymbol{u}^{\infty} = (ex, ey, -2ez). \tag{23}$$

The droplet has viscosity ratio $\lambda = 2$, and capillary number $\mu ec/\gamma = 1$, where c is the minor axis of the spheroid and γ is the surface tension. The surface of the droplet is represented by four-element and ten-element discretizations as described above. Table 2 shows the maximum pointwise error in the velocity evaluated at all points over the surface of the sphere, i.e. the L^{∞} norm. In all cases, the maximum error occurs at the equator where the droplet curvature is the strongest. For reference, the last entry in each column give the actual value of the radial velocity. The spectral element computations yield exponential convergence in all cases.

The results of tables 1 and 2 demonstrate the performance of the spectral boundary element method for flow about individual particles or droplets. In the next test, we consider a flow involving interacting particles in close proximity. The first case considers two spheres of radius c in a squeezing motion with a small gap of size $2h$. Each sphere is discretized by projecting onto the faces of a cube with a single element on five faces and the contact face divided into four equal squares. This yields nine elements per sphere with the point of closest contact at the corner of an element. The error in the dimensionless force is shown in table 3 for gap sizes $h/c = 0.1$ and 0.01. In the absence of an exact solution, the error in each case is estimated by comparing with

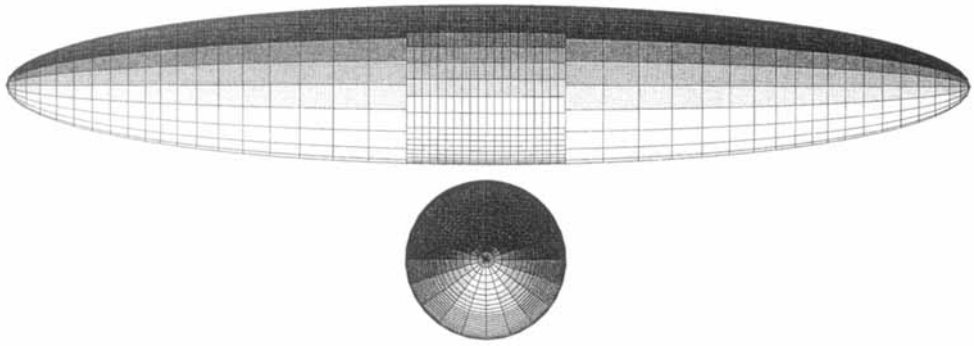

FIGURE 2. Crossed spheroids with aspect ratio of 6:1. Lines show positions of constant ξ and constant η on particle surface.

	Spheres		Spheroids	
N_B	$h/c = 0.10$	$h/c = 0.01$	$h/c = 0.10$	$h/c = 0.01$
4	0.0084404	−49.6616	−0.1073464	−15.2491
5	−0.0015524	−11.9756	−0.0006399	1.2696
6	−0.0003354	−1.1952	0.0004159	0.4666
7	−0.0000245	0.2979	−0.0006665	−0.0777
8	−0.0000071	0.0700	−0.0002113	−0.1712
9	0.0000011	−0.0849	−0.0000421	−0.1033
10	0.0000004	−0.0837	−0.0000062	−0.0493
11	0.0000001	−0.0454	−0.0000004	−0.0247
12	−4.6255420	−0.0183	−16.9038462	−0.0125
13	—	−0.0056	—	−0.0056
14	—	−0.0011	—	−0.0019
15	—	−28.1130	—	−104.0269

TABLE 3. Error in dimensionless force $F/(6\pi\mu cU)$ for two spheroids (minor axis c) separated by a gap $2h$ in squeezing motion with velocity $\pm U$. Spheres are discretized with nine elements per particle, while the 6:1 prolate spheroids employ 16 elements. The table shows an exponential decrease in error with increasing order of the basis N_B. The last value in each column gives the actual force as calculated with that N_B.

the solution for the highest-order basis. The last entry in each column gives the computed value at that N_B. The results for a gap $h/c = 0.1$ show rapid convergence with a relative error of order 2×10^{-6} at $N_B = 11$. The results for the 0.01 gap converge more slowly, but still yield a relative error of order 4×10^{-5} at $N_B = 14$. In this latter case, we have extended the basis up to $N_B = 15$ to demonstrate the reliability for high basis counts. A more effective strategy in this case would be to employ additional elements in the near contact region. The squeezing flow between the two spheres is an example of an axisymmetric flow; however, this feature has not been exploited in the three-dimensional computation.

To confirm that the performance of the spectral element algorithm is not limited to axisymmetric problems, we consider the squeezing motion between a pair of crossed prolate spheroids as illustrated in figure 2. Each spheroid is discretized with 16 elements by projecting onto the sides and ends of a cylinder. Figure 2 illustrates that the spectral boundary elements may be *non-conforming*, i.e. the corner of one element may fall along the side of an adjoining element, and the nodes need not coincide. The panel

layout on the cylinder is similar to that illustrated in figure 2 of the companion paper (Higdon & Muldowney 1995). We have selected an aspect ratio of 6:1 to correspond to the particles employed in the many-body simulations of Claeys & Brady (1993*a*, *b*, *c*). Table 3 shows the error in the resistance force for gaps of size $h/c = 0.1$ and 0.01 where c is the minor axis of the spheroid. The larger gap shows a relative error of order 2×10^{-8} at $N_B = 11$, while the smaller gap shows slower convergence with a relative error of 2×10^{-5} at $N_B = 14$. Each of these results demonstrates excellent convergence for a problem involving slender particles with small lubrication layers. The performance in this case shows the effectiveness of placing smaller elements near the lubrication zone. Overall, the results of table 3 provide further confirmation of the reliability of spectral element formulations based on integral equations of the first kind.

The numerical examples discussed above are sufficient to demonstrate the viability of the spectral boundary element method for the three-dimensional Stokes equations. There are however, additional concerns for the fluid dynamicists who would employ these algorithms in Stokes flow applications. These concerns include the presence of boundary walls for interior flows, the imposition of boundary conditions in periodic domains, the presence of piecewise continuous boundaries with intersecting surfaces, and the presence of stress singularities at boundary edges or cusps. In addition, free surface flows often lead to droplets of distorted shape which present greater challenges than the simple shapes analysed above. We shall address these concerns in the sections below, studying rigid domains in §6 and free surface flows in §7. Our goals are to demonstrate the reliability of the spectral boundary element algorithm in more complicated flows and to establish benchmarks for others who would develop advanced computational methods for three-dimensional Stokes flow. In pursuit of these goals, we might select any number of artificial model geometries; however, we find it more satisfying to consider well-characterized problems which yield physically meaningful results for the fluid dynamics researcher.

6. Periodic domains – discontinuous surfaces

To validate the performance of the spectral boundary element algorithm across a wider range of flows, we consider applications involving non-smooth boundary shapes, periodic domains and interior flows. To illustrate these applications, we consider two geometries which model permeable membranes and interlaced fibre screens employed in chemical engineering processes. Solid membranes with circular pores of equal sizes are employed in particle size analysis and separation, while screens are commonly employed as sieves or as collection devices in filtration systems. These models provide useful results for the engineering applications, but also introduce new features which test the spectral boundary element algorithm. These features include periodic domains, integral equations with mixed velocity–force boundary conditions, intersecting rigid surfaces (screens) and singular stresses associated with sharp boundaries (membranes). In all cases, we shall see that the spectral boundary element method shows rapid convergence with excellent accuracy.

We begin by considering the fluid flow through a model screen. We suppose that the screen is composed of a periodic square grid of intersecting cylinders of radius a. Far from the screen, the fluid is maintained at constant pressure with a pressure drop across the screen of Δp. The dimensionless permeability (or mobility) of the screen is defined with respect to the length L by

$$K_L = \frac{\mu Q}{\Delta p L^3}, \tag{24}$$

where Q is the volume flow rate through one unit cell, and L is the wavelength of the periodic grid.

For the boundary integral calculation, we define a computational domain consisting of a single periodic cell extending in the vertical direction from $z = +H$ to $-H$ above and below the centreplane of the screen. The boundary conditions are no-slip on the surfaces of the cylinders, periodicity on the sides of the cell and infinity conditions $f_x = 0, f_y = 0, f_z = \pm\Delta p/2$ on the top and bottom boundaries. With these boundary conditions, numerous tests were conducted to test the sensitivity of the permeability K_L to the height of the finite domain. These tests showed that $H = 4L$ is sufficient to guarantee a relative error in K_L of less than 1×10^{-5} compared with the limit $H \to \infty$.

Two different boundary discretizations were employed for the spectral element method. For large fibres with $2a/L = 0.5$ to 0.98, the top half of the domain was discretized with one element on the top and centreplane boundaries, one element on each sidewall and one element on each quarter-cylinder for a total of ten elements. For small fibres with $2a/L = 0.001$ to 0.5 an additional element was added to each sidewall to give more resolution near the fibre. A total of 22 elements was used over the entire domain. In each case, symmetry about the planes $x = 0$, $y = 0$, $x = y$, $z = 0$ was employed to reduce the number of unknowns. For small fibres, the volume flow was evaluated by integrating over the top surface element. For very large fibres near the limit $2a/L \to 1$, the integral over the small open area at the centreplane yielded more accurate results.

Table 4 shows the convergence of the spectral element computations for fibres of radius $2a/L = 0.01$ and 0.95 as a function of the basis order N_B. In each case, exponential convergence is achieved with relative errors at $N_B = 11$ of 6×10^{-5} and 7×10^{-4} respectively. Intermediate values of radius yield even more rapid convergence, e.g. $2a/L = 0.50$ has an error of 8×10^{-7} at $N_B = 11$. This performance is quite good, given the non-smooth character of the surface stress in the corners created by the intersecting cylinders. Table 5 presents the permeability as a function of cylinder radius for fibres from $2a/L = 0.001$ to 0.98. Convergence tests for each value were performed to verify the numbers to the stated precision. As an independent test, lubrication theory analogous to that employed by Chapman & Higdon (1992) was employed to verify the value of K_L as $2a/L \to 1$.

The permeability data presented in table 5 are the most useful macroscopic data for engineering applications. We note however, that the current algorithm also provides a simple and efficient approach to computing the entire microscopic flow field. One may discretize the volume of a unit cell by employing three-dimensional spectral elements or a simple Cartesian mesh. Interior integrals (12) may be evaluated at the grid points and these data employed to interpolate to any additional points. With this approach, the computed flow fields are readily accessible for further studies involving particle trajectories or alternative Lagrangian simulations.

Our second example for periodic domains with non-smooth boundaries consists of a zero-thickness membrane with a periodic network of circular pores. We assume a square two-dimensional array in the (x, y)-plane with wavelength L and pore radius b. As before, we chose a single unit cell for the computational domain, extending from $z = -H$ to $+H$. A value $H = 4L$ is sufficient to guarantee a relative error of less than 4×10^{-4} compared with the result for $H \to \infty$. For the circular pores, we exploit symmetry about the plane $z = 0$ and discretize only the top half of the domain. The boundary conditions on the top and sides of the unit cell are as discussed above, and the no-slip condition applies on the solid part of the membrane. From symmetry, the boundary conditions on the open pore surface are $u_x = 0$, $u_y = 0$, $f_z = 0$. The domain

N_B	$2a/L = 0.01$	$2a/L = 0.95$	$2b/L = 0.01$	$2b/L = 0.95$
3	—	—	-7.5×10^{-2}	5.6×10^{-2}
4	1.0×10^{-3}	-3.1×10^{-1}	-3.9×10^{-3}	-8.5×10^{-3}
5	2.4×10^{-3}	-1.7×10^{-1}	-7.1×10^{-3}	-1.1×10^{-2}
6	1.9×10^{-3}	-6.0×10^{-2}	-3.8×10^{-3}	-3.3×10^{-3}
7	1.2×10^{-3}	6.6×10^{-3}	-1.8×10^{-3}	1.3×10^{-3}
8	7.3×10^{-4}	2.3×10^{-2}	-8.3×10^{-4}	9.3×10^{-4}
9	3.9×10^{-4}	1.4×10^{-2}	-4.1×10^{-4}	-7.1×10^{-4}
10	1.9×10^{-4}	4.4×10^{-3}	-1.8×10^{-4}	-4.1×10^{-4}
11	6.9×10^{-5}	7.3×10^{-4}	-8.7×10^{-5}	-6.6×10^{-5}

TABLE 4. Error in permeability for screens and porous membranes as a function of increasing order of basis N_B. The table shows the error relative to the exact value for two choices of fibre radius a for screens, and pore size b for porous membranes.

$2a/L$	$\mu Q/\Delta p L^3$	$2b/L$	$\mu Q/\Delta p b^3$
0.001	0.2452	—	—
0.005	0.17985	—	—
0.01	0.151 59	0.01	0.3333
0.02	0.123 23	—	—
0.05	$0.856\,30 \times 10^{-1}$	0.05	0.3334
0.10	$0.574\,908 \times 10^{-1}$	0.10	0.3335
0.20	$0.308\,945 \times 10^{-1}$	0.20	0.3340
0.30	$0.173\,283 \times 10^{-1}$	0.30	0.3356
0.40	$0.944\,514 \times 10^{-2}$	0.40	0.3388
0.50	$0.478\,129 \times 10^{-2}$	0.50	0.3445
0.60	$0.213\,076 \times 10^{-2}$	0.60	0.3537
0.70	$0.765\,181 \times 10^{-3}$	0.70	0.3687
0.80	$0.183\,128 \times 10^{-3}$	0.80	0.3934
0.90	$0.160\,77 \times 10^{-4}$	0.90	0.4381
0.95	$0.141\,76 \times 10^{-5}$	0.95	0.4783
0.98	0.572×10^{-7}	—	—

TABLE 5. Dimensionless permeability for screens of intersecting cylinders and for porous membranes. The table shows $\mu Q/\Delta p L^3$ for screens with cylinder radius a, grid wavelength L, and $\mu Q/\Delta p b^3$ for membranes with circular pores of radius b, grid wavelength L. All data accurate to ± 1 in the last figure, except ± 2 where last figure is underlined.

is discretized with 17 elements, with one element on the top, and one element on each of the sidewalls. The circular pore is divided into four sectors with one element per sector. The solid part of the membrane is divided into eight elements with a thin four-element rim bordering the pore and four thicker outer elements extending to the edge of the unit cell. The basis points on the inner rim are stretched toward the pore edge to give additional resolution to resolve the singular shear stress at the pore's edge.

In the limit as the pore radius approaches zero, $2b/L \to 0$, the solution for the pore approaches Sampson's solution for an isolated pore in an infinite plane (see Happel & Brenner 1973, p. 153):

$$Q = \Delta p b^3/(3\mu). \tag{25}$$

Thus, we define the dimensionless permeability K_b

$$K_b = \mu Q/(\Delta p b^3), \tag{26}$$

whose value approaches 1/3 as the pore radius approaches zero.

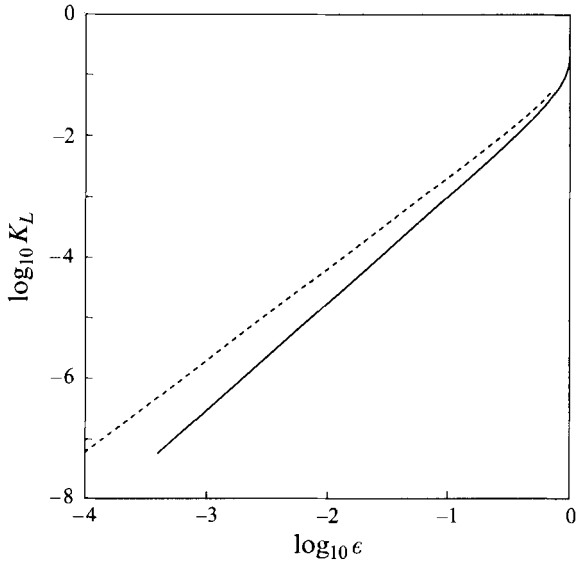

FIGURE 3. Permeability $K_L = \mu Q/(\Delta p\, L^3)$ versus surface porosity ϵ for two model filters: solid line, grid of intersecting cylinders; dashed line, circular pores in zero-thickness membrane.

Table 4 shows the convergence of the permeability as a function of N_B for pore sizes $2b/L = 0.01$ and 0.95. The accurate prediction of the permeability for the pore membrane presents a challenge for the numerical computation due to the singular stress at the pore's edge. Nonetheless, the results for $N_B = 11$ have converged in each case with a relative error of order 1×10^{-4}. Table 5 presents the permeability K_b as a function of pore radius $2b/L$. These data show the departure from the Sampson asymptote $K_b = 1/3$ as the pore size increases.

The excellent accuracy of the spectral results in the presence of the singular stresses is attributable to the mapping which stretches basis points toward the singular edge. The stress at the sharp edge has an $x^{-1/2}$ singularity (Moffatt 1964), while the basis point mapping is locally $x \sim \xi^2$. While the polynomial discretization cannot resolve the singularity itself, the integral contribution $\sim x^{-1/2}\,\mathrm{d}x \sim \mathrm{d}\xi$ is bounded and is well represented by the spectral element discretization. The application of mappings in the basis variables ξ or η is one technique for dealing with singularities in the stress field. A second technique (*hp* refinement) is to decrease the size of the local element as the order of the basis is increased. We have had similar success with this technique, however, it typically requires a few additional elements and slightly higher computational cost for the same accuracy.

We close this section with a comparison between the properties of the two filter models. Owing to the difference in the geometrical parameters a and b, we require a new parameter to compare the models on a common basis. We choose the surface porosity ϵ defined as the open area divided by total area in the centreplane on the filter. The dimensionless permeability K_L versus ϵ for the two filters is plotted in figure 3. Note that the circular pore membrane has greater permeability for all values of surface porosity. This is due to the greater concentration of solid area in the corners of the unit cell, while the fibre screen tends to distribute the area more uniformly. It is well known in studies of fibrous media (Jackson & James 1986) that a more uniform surface distribution leads to lower permeability.

7. Free surface flows

As a final test of the spectral boundary element algorithm, we return to equation (8) and consider free surface flows associated with droplet deformation. Our goal is to test the algorithm for more complex surface shapes and to assess the performance for flows driven by surface tension. For such flows, the jump in surface stress is proportional to the local surface curvature (div $\boldsymbol{n}$) which requires second derivatives of the boundary geometry. Low-order methods (up to second order) yield discontinuous curvatures requiring special care in implementing the jump stress boundary conditions. By contrast, the high-order spectral basis yields a smooth curvature distribution with accuracy of order (N_G-2). As test case, we consider the non-axisymmetric instability of a toroidal droplet due to the interaction of gravitational and surface forces.

When a non-buoyant viscous drop settles through a viscous fluid under conditions of weak surface tension, it may undergo an instability which leads to the formation of an open toroidal droplet (Kojima, Hinch & Acrivos 1984). The axisymmetric toroidal droplet may undergo further instabilities leading to variation in the cross-sectional radius and displacement of the torus centreline from the horizontal plane. In the later stages, these instabilities may lead to saddle-shaped droplets as shown in figure 4 of Kojima *et al.* Those authors present a theory for the axisymmetric evolution of the droplet leading up to a thin toroidal shape, but do not address the non-axisymmetric evolution in the later stages. In the present section, we discuss results for the instantaneous velocity field associated with a deformed toroidal droplet and identify the basic mechanisms leading to the long-term droplet shape. In a future effort, we shall present results for a full time dependent simulation of this instability.

We consider a toroidal droplet of viscosity $\lambda\mu$ and surface tension γ with density ρ_D settling through a fluid of density ρ and viscosity μ. The deformed droplet surface is defined by

$$\left.\begin{aligned} x &= b\cos\theta+(a+\eta\sin m\theta)\cos\phi\cos\theta,\\ y &= b\sin\theta+(a+\eta\sin m\theta)\cos\phi\sin\theta,\\ z &= (a+\eta\sin m\theta)\sin\phi, \end{aligned}\right\} \tag{27}$$

where a is the unperturbed core radius, b is the torus radius, η is the amplitude of the core perturbation, m is the perturbation wavenumber and θ and ϕ are parametric angles in $(0,\ 2\pi)$ defining the surface position. A three-dimensional view of the deformed droplet is shown in figure 4.

To characterize the deformation and settling velocity of the droplet, we define three average velocities. The first is the volume average velocity of the droplet:

$$\bar{u}_i = \int_V u_i\,\mathrm{d}V \Big/ \int_V \mathrm{d}V \equiv \int_S x_i u_j n_j\,\mathrm{d}S \Big/ \frac{1}{3}\int_S x_j n_j\,\mathrm{d}S. \tag{28}$$

By symmetry and reversibility of Stokes flow, the only non-zero component is the vertical velocity component $\bar{u}_z$.

Next, we consider a given cross-section of the droplet at a plane $\theta=\theta_0$, and define the velocity $\tilde{u}_i$ of the centroid at that cross-section. This may be expressed as

$$\tilde{u}_i = \int_C (x_i-\tilde{x}_i)\,u_j n_j\,\mathrm{d}s \Big/ \frac{1}{2}\int_C (x_j-\tilde{x}_i)\,n_j\,\mathrm{d}s, \tag{29}$$

where C denotes the perimeter and $\tilde{x}_i$ the centroid of the cross-section.

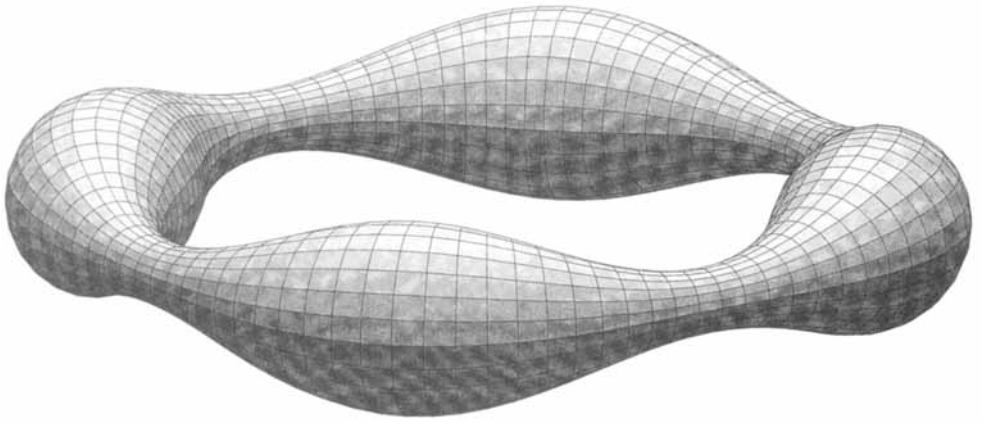

FIGURE 4. Three-dimensional view of deformed torus described by equation (27) with parameters $a = 1$, $b = 6$, $\eta = 0.5$, $m = 4$. Lines show positions of constant ξ and constant η on particle surface.

	Gravity flow		Surface tension flow		
N_B	$\lvert\boldsymbol{u}_{err}\rvert$	$\bar{u}_z$	$\lvert\boldsymbol{u}_{err}\rvert$	$\tilde{u}_{nMAX}$	$\tilde{u}_{rMAX}$
4	0.042696	0.047865	0.028236	−0.007821	0.006103
5	0.020021	−0.002077	0.036412	−0.006561	−0.002850
6	0.005331	−0.001547	0.002687	0.000805	−0.000413
7	0.000662	0.000008	0.001666	0.000387	0.000260
8	0.000730	0.000024	0.000238	0.000052	0.000005
9	0.000443	0.000000	0.000138	0.000010	−0.000006
10	0.000177	0.000000	0.000045	−0.000009	−0.000001
11	0.000090	0.000000	0.000009	−0.000003	−0.000001
12	—	−1.309090	—	0.010867	0.035580

TABLE 6. Error in surface velocity for a deformed toroidal drop illustrated in figure 4. Droplet shape defined by (27) with parameters: $a = 1$, $b = 6$, $\eta = 0.5$, $m = 4$. Velocities $\lvert\boldsymbol{u}_{err}\rvert$ are maximum pointwise errors over the droplet surface for the respective flows. Mean settling velocity $\bar{u}_z$ is average over volume of droplet, non-dimensionalized with respect to $\Delta\rho a^2/\mu$. Radial and normal velocities $\tilde{u}_r$ and $\tilde{u}_n$ are averaged over the cross-section and non-dimensionalized with respect to γ/μ. The table shows a decrease in velocity error with increasing order of basis N_B. The last entry in each column shows actual velocity evaluated with $N_B = 12$. Subscript MAX indicates the velocity evaluated at cross-section of maximum radius.

Finally, we characterize the growth rate of the core radius by defining the average normal velocity at the cross-section:

$$\tilde{u}_n = \int_C u_j n_j \, \mathrm{d}s \Big/ \int_C \mathrm{d}s. \tag{30}$$

For the spectral boundary element computations, the borders of the elements are laid out at equal intervals of θ and ϕ with two elements in the ϕ-direction and two elements per wavelength in the θ-direction. Numerous convergence tests were conducted to test the performance of the spectral element code and to verify the accuracy of the results. Table 6 shows the convergence results for a droplet with perturbation wave number $m = 4$ with radius $b/a = 6$ and amplitude $\eta/a = 0.5$. The deformation for this droplet is illustrated in figure 4. In table 6, we tabulate independent error measures for the gravity- and surface-tension-driven flows. We present results for the maximum pointwise error in $\boldsymbol{u}$ over the entire surface, as well as

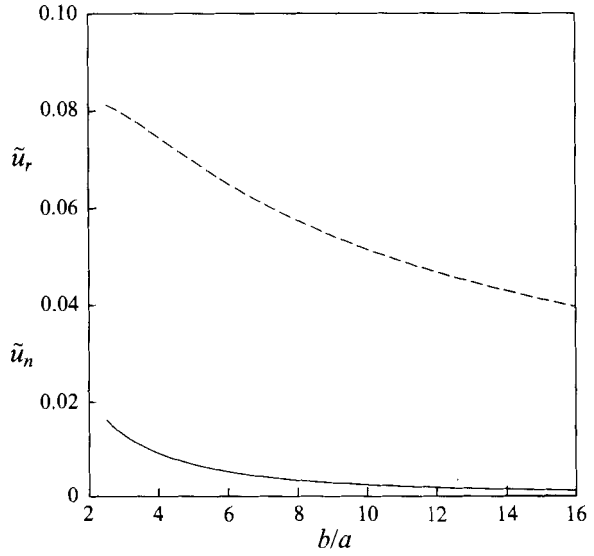

FIGURE 5. Surface velocity of an unperturbed toroidal droplet with viscosity ratio $\lambda = 2$ as a function of torus radius b/a. Velocity non-dimensionalized as $\mu u/\gamma$. Solid line, mean normal velocity $\tilde{u}_n$ as defined by (30); dashed line, mean radial velocity $\tilde{u}_r$ as defined by (29).

the errors in the mean velocity of the droplet $\bar{u}_z$, the radial velocity of the centroid $\bar{u}_r$ and the mean normal velocity $\tilde{u}_n$. The latter quantities are evaluated at the cross sections of maximum radius. (Cross-sections of minimum radius show comparable results.) In all cases, the spectral element computations yield excellent accuracy with exponential convergence. The overall errors in the mean velocities are roughly an order of magnitude smaller than the maximum pointwise errors. The errors in the pointwise and mean velocities for the surface tension flow confirm the accuracy of the algorithm in evaluating curvature effects for complex surface shapes.

With a reliable technique for computing the velocity fields in hand, we turn our attention to the physical mechanisms governing this phenomenon. Owing to the symmetry of the imposed perturbation, the gravitational and surface tension driving forces act independently in the instantaneous velocity field. The interaction of these effects occurs in the subsequent evolution when the vertical symmetry is broken. In figure 5, we examine the radial and normal velocity induced by the surface tension for an undeformed droplet with $\eta = 0$. In this case, the surface tension causes the drop to pull inward with a negative radial velocity $\tilde{u}_r$ and an increasing core radius with positive $\tilde{u}_n$. For an incompressible fluid, the volume of the droplet is fixed ($V = 2\pi a^2 b$), and the two velocities are related by $\tilde{u}_r = -2\tilde{u}_n b/a$. For larger torus radius b, the magnitude of both velocities decreases owing to the reduction of curvature in the longitudinal direction.

Next we examine the radial and normal velocity for a deformed droplet as a function of torus radius (figures 6*a*, *b*). In each case, we plot the difference in velocity between the cross-sections of maximum and minimum core radius. The velocity differences illustrate the growth rate of the varicose instability. Results are shown for wavenumbers $m = 1, 2, 3, 4$ with amplitude $\eta/a = 0.1$. We begin by considering the normal velocity difference in figure 6(*a*). For the $m = 1$ and $m = 2$ perturbations, the disturbance is unconditionally unstable for all torus radii b/a. For these droplets, the curvature associated with the varicosity dominates, squeezing the fluid out of the constrictions

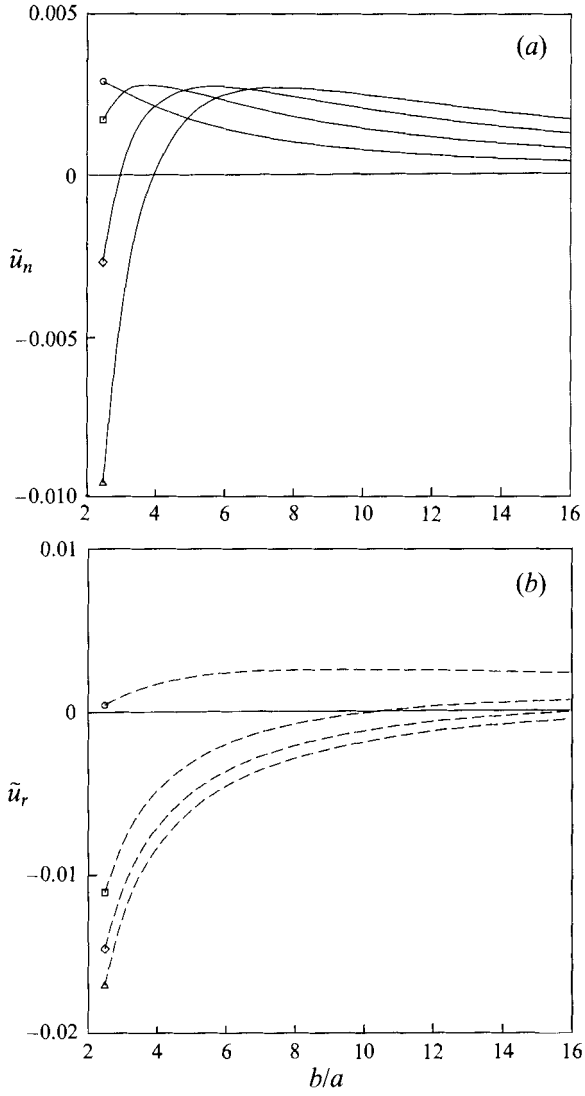

FIGURE 6. Surface velocity of perturbed toroidal droplet with viscosity ratio $\lambda = 2$, perturbation amplitude $\eta/a = 0.1$, versus torus radius b/a. Velocity non-dimensionalized as $\mu u/\gamma$. (*a*) Difference in mean normal velocities $\tilde{u}_n$ at maximum and minimum cross-sections. (*b*) Difference in mean radial velocities $\tilde{u}_r$ at maximum and minimum cross-sections. Symbols identify curves for different wavenumbers: ○, $m = 0$; □, $m = 1$; ◇, $m = 3$; △, $m = 4$.

and into the bulges on the droplet. For the $m = 3$ and $m = 4$ perturbations, the droplet is unstable for long waves when b/a is large, but is stable for short waves associated with small b/a. In these cases, the curvature in the longitudinal direction dominates, pulling the constriction toward its undisturbed position. This behaviour is analogous to that in the classic Rayleigh analysis of an axisymmetric liquid thread. The difference in the radial velocities is plotted in figure 6(*b*). In this figure, both positive and negative velocities displace the centroids from the initial circular path inducing an additional mechanism of instability.

Figure 7 illustrates the effect of perturbation amplitude on the disturbance evolution. We show the difference in normal velocity at maximum and minimum cross-sections

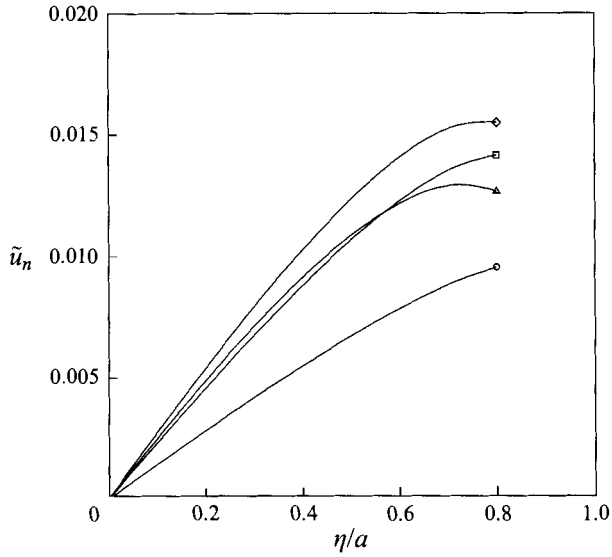

FIGURE 7. Mean normal velocity $\tilde{u}_n$ of perturbed toroidal droplet with viscosity ratio $\lambda = 2$, torus radius $b/a = 6$, as function of perturbation amplitude η/a. Velocity non-dimensionalized as $\mu u/\gamma$. Symbols identify curves for different wavenumbers: ○, $m = 0$; □, $m = 1$; ◇, $m = 3$; △, $m = 4$.

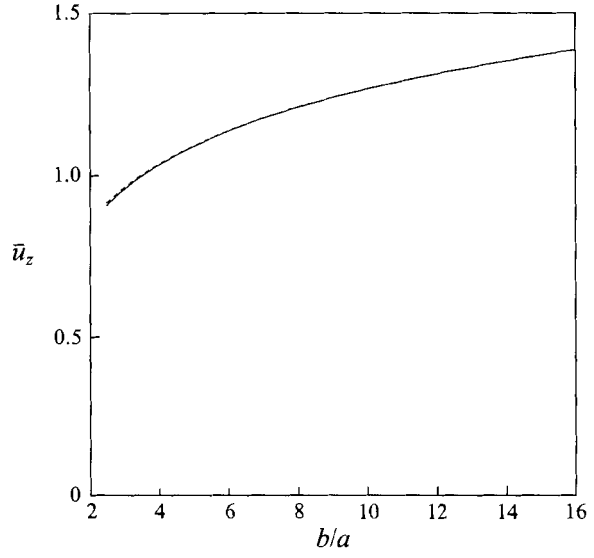

FIGURE 8. Mean settling velocity $\bar{u}_z$ of an unperturbed toroidal droplet with viscosity ratio $\lambda = 2$ as a function of torus radius b/a. Velocity non-dimensionalized as $\mu u/\Delta\rho g a^2$. Solid line, computed velocity; dashed line, slender body theory (31) of Kojima *et al.* (1984).

for tori with radius $b/a = 6$. At small amplitudes, all curves are in agreement with linear theory showing a linear growth of velocity with amplitude. Each begins to show signs of saturation at the highest amplitude with the strongest decline for the $m = 4$ perturbation. At these large amplitudes, the constrictions become quite small, and the volume of fluid which is displaced from them is insufficient to greatly affect the radii of the bulges.

Having illustrated the basic mechanisms responsible for the surface tension

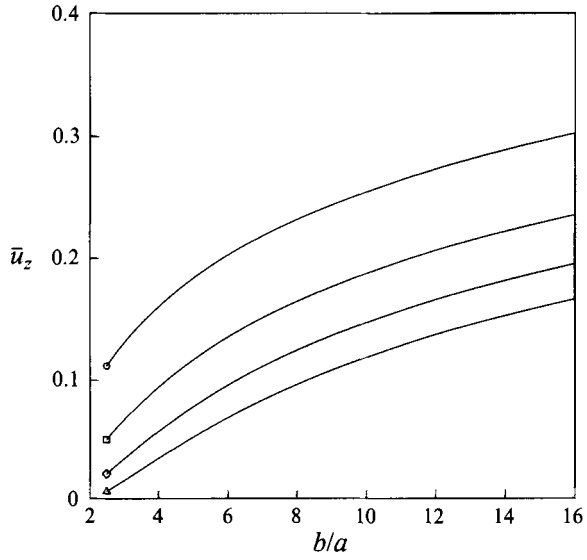

FIGURE 9. Settling velocity of perturbed toroidal droplet with viscosity ratio $\lambda = 2$, perturbation amplitude $\eta/a = 0.1$ versus torus radius b/a. Velocity non-dimensionalized as $\mu u/\Delta\rho g a^2$. Plotted quantity is difference in settling velocities $\tilde{u}_z$ at maximum and minimum cross-sections for wavenumbers: ○, $m = 0$; □, $m = 1$; ◇, $m = 3$; △, $m = 4$.

instability, we turn next to the gravitational effects which are responsible for the saddle shapes observed in experiments. First, we plot the settling velocity of an unperturbed torus as a function of radius b/a, figure 8. The settling velocity increases monotonically with increasing radius b for fixed core radius a. This is easily explained because the gravitational driving force per unit length is fixed while the drag force decreases as the body becomes more slender. The computed settling velocity may be compared with that predicted by slender body theory (Kojima *et al.* 1984):

$$u_z = \frac{\Delta\rho g a^2}{\mu} \frac{(1+\lambda)\ln(8b/a) + 1 + \frac{1}{2}\lambda}{4(1+\lambda)}, \tag{31}$$

showing excellent agreement over the entire range of radii.

In figure 9, we examine the difference in centroid velocities $\tilde{u}_z|_{MAX} - \tilde{u}_z|_{MIN}$ between the cross-sections of maximum and minimum radius. In all cases, the bulges settle more rapidly than the constrictions owing to the greater concentration of dense fluid. Effectively, the bulges are equivalent to dense droplets of larger radius, and the settling velocity is proportional to the square of droplet radius. For high wavenumbers m, the bulges and constrictions are closer together yielding a smaller velocity differential compared with the low-wavenumber disturbances. The $m = 1$ perturbation yields the largest velocity giving rise to the most rapid deformation of the ring. The $m = 2$ perturbation leads to the saddle shape observed in the experiments of Kojima *et al.* while higher modes yield more elaborate shapes. Note that the vertical settle velocities are not the decisive factor in determining the most unstable mode of the instability. The dominant mechanism is the varicose instability associated with surface tension, while the gravitational deflection occurs after the basic instability has been established. In the absence of surface tension and perturbations of core radius, vertical displacements of the core centerline would show no growth owing to gravitational settling. This result may be inferred from the reversibility of low Reynolds number flow.

For any given torus, the most unstable mode will be determined by the normal velocity plotted in figure 6(*a*). For the thickest tori, the $m = 1$ mode is favoured, while for more slender droplets, higher modes are favoured, first $m = 2$, followed by $m = 3$, etc. Thus, we should expect more elaborate deformations as the torus becomes more slender. In this discussion, we have assumed the initial existence of a droplet of toroidal shape. It should be noted that the development of tori beyond a certain slenderness ratio b/a requires inertial effects or an imposed straining field to overcome the dilating effect of surface tension. In the absence of such effects, the torus radius will contract and the core radius will increase as shown in figure 5.

8. Conclusions

In this paper, we have introduced a new approach for boundary integral computations for low Reynolds number flow. We have demonstrated the accuracy and efficiency of this algorithm for equations of the first kind and of the second kind. We have considered geometries with extreme aspect ratios, small lubrication layers, intersecting surfaces, cusped boundaries and periodic as well as infinite domains. We have considered a number of applications in Stokes flow with application to particle mobility, droplet deformation and flow through membranes. In a further application of these techniques (Higdon & Muldowney 1995), we compute the resistance functions for spherical particles, drops and bubbles in a cylindrical domain.

The spectral boundary element algorithm presented in this paper provides the basis for a new class of boundary integral algorithms. The introduction of a spectral basis facilitates a number of additional refinements analogous to those employed with spectral finite element algorithms. While we have utilized the same order basis in each variable and on each element, self-adaptive methods may be employed which adjust the order of the basis according to local requirements. For this purpose, the spectral basis provides a simple error estimate based on the computed coefficients of the orthogonal polynomials. The use of non-conforming elements and degenerate quadrilaterals is of significant interest in the finite element literature owing to the increased flexibility in domain discretization. These features are an integral part of the present algorithm as demonstrated in §5. Iterative solutions and multigrid methods are the subject of much interest in both the boundary integral and spectral element literature. The spectral boundary element algorithm provides an efficient platform for the implementation of these techniques. Specifically, we note that lower order representations for 'coarse' grid iterations may be extracted from the high-order system matrices with no additional numerical integration. This is a standard feature of spectral element discretizations. The implementation of these ideas as well as other refinements will be the subject of future efforts in this area.

This work was supported by the National Science Foundation. A part of the computations for this paper was carried out at the National Center for Supercomputing Applications at the University of Illinois. G. P. Muldowney acknowledges fellowship support from the Fannie and John Hertz Foundation.

REFERENCES

Alarcon, E. & Reverter, A. 1986 *p*-adaptive boundary element. *Intl J. Numer. Meth. Engng* **23**, 801–829.

Braß, H. & Hammerlin, G. 1982 *Numerical Integration III.* Birkhauser.

CANUTO, C., HUSSAINI, M. Y., QUARTERONI, A. & ZANG, T. A. 1988 *Spectral Methods in Fluid Dynamics*. Springer.

CANUTO, C. & QUARTERONI, A. 1988 *Spectral and Higher Order Methods for Partial Differential Equations*. North-Holland: Elsevier.

CERROLAZA, M. & ALARCON, E. 1987 P-adaptive boundary elements for three dimensional potential problems. *Commun. Appl. Numer. Meth.* **3**, 335–344.

CERROLAZA, M. & ALARCON, E. 1989 Further applications of P-adaptive boundary elements. In *Boundary Elements X*.

CHAPMAN, A. M. & HIGDON, J. J. L. 1992 Oscillatory Stokes flow in periodic porous media. *Phys. Fluids* A **4**, 2099–2116.

CHAN, C. Y., BERIS, A. N. & ADVANI, S. G. 1992 Second order boundary element method calculations of hydrodynamic interactions between particles in close proximity. *Intl J. Numer. Meth. Fluids* **14**, 1063–1086.

CLAEYS, I. L. & BRADY, J. F. 1993*a* Suspensions of prolate spheroids in Stokes flow. Part 1. Dynamics of a finite number of particles in an unbounded fluid. *J. Fluid Mech.* **251**, 411–442.

CLAEYS, I. L. & BRADY, J. F. 1993*b* Suspensions of prolate spheroids in Stokes flow. Part 2. Statistically homogeneous dispersions. *J. Fluid Mech.* **251**, 443–477.

CLAEYS, I. L. & BRADY, J. F. 1993*c* Suspensions of prolate spheroids in Stokes flow. Part 3. Hydrodynamic transport properties of crystalline dispersions. *J. Fluid Mech.* **251**, 479–500.

DUFFY, M. G. 1982 Quadrature over a pyramid or cube of integrands with a singularity at a vertex. *J. Numer. Anal.* **19**, 1260–1262.

ESPELID, T. O. & GENZ, A. 1992 *Numerical Integration: Recent Developments, Software and Applications*. Kluwer.

GOTTLIEB, D. & ORSZAG, S. A. 1984 *Numerical Analysis of Spectral Methods: Theory and Applications*. SIAM.

GUO, B. Q., PETERSDORFF, T. VON & STEPHAN, E. P. 1990 An h-p version of BEM for plane mixed boundary value problems. In *Advances in Boundary Elements*.

HAMMERLIN, G. 1979 *Numerische Integration*. Birkhauser.

HAMMERLIN, G. 1982 *Numerical Integration*. Birkhauser.

HAPPEL, J. & BRENNER, H. 1973 *Low Reynolds Number Hydrodynamics*. Noordhoff.

HAYAMI, K. 1992 *A Projection Transformation Method for Nearly Singular Surface Boundary Element Integrals*. Springer.

HEBEKER, F. K. 1986 Efficient boundary element methods for three dimensional exterior viscous flows. *Num. Meth. Partial Diff. Equats.* **2**, 273–297.

HEBEKER, F. K. 1988 On the numerical treatment of viscous flows against bodies with corners and edges by boundary element and multigrid methods. *Numer. Meth.* **52**, 81–99.

HIGDON, J. J. L. 1985 Stokes flow in arbitrary two-dimensional domains: shear flow over ridges and cavities. *J. Fluid Mech.* **159**, 195–226.

HIGDON, J. J. L. 1990 Effects of pressure gradients on Stokes flow over cavities. *Phys. Fluids* A **2**, 112–114.

HIGDON, J. J. L. 1993 The kinematics of the four roll mill. *Phys. Fluids* A **5**, 274–276.

HIGDON, J. J. L. & MULDOWNEY, G. P. 1995 Resistance functions for spherical particles, droplets and bubbles in cylindrical tubes. *J. Fluid Mech.* **298**, 193–210.

HIGDON, J. J. L. & SCHNEPPER, C. A. 1994 High order boundary integral methods for viscous free surface flows. In *Free Boundaries in Viscous Flows*. Springer.

HINCH, E. J. 1972 Note on the symmetries of certain material tensors for a particle in Stokes flow. *J. Fluid Mech.* **54**, 423–425.

HSIAO, G. C. 1988 On the stability of boundary element methods for integral equations of the first kind. In *Boundary Elements IX*, pp. 177–192.

INGBER, M. S. & MONDY, L. A. 1993 Direct second kind boundary integral formulation for Stokes flow problems. *Comput. Mech.* **11**, 11–27.

ISAACSON, E. & KELLER, H. B. 1966 *Analysis of Numerical Methods*. Wiley.

JACKSON, G. W. & JAMES, D. F. 1986 The permeability of fibrous porous media. *Can. J. Chem. Engrs* **64**, 364–374.

KIM, S. & KARRILA, S. 1991 *Microhydrodynamics: Principles and Selected Applications.* Butterworth-Heinemann.

KOJIMA, M., HINCH, E. J. & ACRIVOS, A. 1984 The formation and expansion of a toroidal drop moving in a viscous fluid. *Phys. Fluids* **27**, 19–32.

LARSON, R. E. & HIGDON, J. J. L. 1986 Microscopic flow near the surface of two-dimensional porous media. Part 1. Axial flow. *J. Fluid Mech.* **166**, 449–472.

LARSON, R. E. & HIGDON, J. J. L. 1987 Microscopic flow near the surface of two-dimensional porous media. Part 2. Transverse flow. *J. Fluid mech.* **178**, 119–136.

LI, X. Z., BARTHES-BIESEL, D. & HELMY, A. 1988 Large deformations and burst of a capsule freely suspended in an elongational flow. *J. Fluid Mech.* **187**, 179–196.

LORENTZ, H. A. 1907 Ein allgemeiner satz, die bewegung einer reibenden flussigkeit betreffend, nebst einigen andwendungendesselben. *Abhand. Theor. Phys.* **1**, 23–42.

LYNESS, J. N. 1992 On handling singularities in finite elements. In *Numerical Integration: Recent Developments, Software and Applications* (ed. T. O. Espelid & A. Genz). Kluwer.

MADAY, Y. & PATERA, A. T. 1989 Spectral element methods for the incompressible Navier–Stokes equations. In *State of the Art Surveys in Computational Mechanics* (ed. A. K. Noor & J. T. Oden). ASME.

MOFFATT, H. K. 1964 Viscous and resistive eddies near a sharp corner. *J. Fluid Mech.* **18**, 1–18.

MULDOWNEY, G. P. 1988 PhD dissertation, University of Illinois.

OCCHIALINI, J. M. & HIGDON, J. J. L. 1992 Convective mass transport from rectangular cavities in viscous flow. *J. Electrochem. Soc.* **10**, 2845–2855.

OCCHIALINI, J. M., MULDOWNEY, G. P. & HIGDON, J. J. L. 1992 Boundary integral/spectral element approaches to the Navier–Stokes equations. *Intl J. Numer. Meth. Fluids.* **15**, 1361–1381.

PARRIERA, P. 1988 Self-adaptive hierarchical boundary elements in elastostatics. In *Boundary Elements IX.*

PHAN-THIEN, N., TRAN-CONG, T. & RAMIA, M. 1987 A boundary element analysis of flagellar propulsion. *J. Fluid Mech.* **184**, 533–549.

POWER, H. & MIRANDA, G. 1987 Second kind integral equation formulation of Stokes flow past a particle of arbitrary shape. *SIAM J. Appl. Maths* **47**, 689–698.

POZRIKIDIS, C. 1990 The axisymmetric deformation of a red blood cell in a uniaxial strining Stokes flow. *J. Fluid Mech.* **216**, 231.

POZRIKIDIS, C. 1992 *Boundary Integral and Singuarlity Methods for Linearized Viscous Flow.* Cambridge University Press.

RALLISON, J. M. 1984 The deformation of small viscous drops and bubbles in shear flows. *Ann. Rev. Fluid Mech.* **16**, 45–66.

RANK, E. 1988 Adaptive boundary element methods. In *Boundary Elements IX.*

SCHNEPPER, C. A. 1988 Application of the boundary integral method to the deformation of droplets in viscous flow. MS thesis, University of Illinois.

STONE, H. A. 1994 Dynamics of drop deformation and breakup in viscous fluids. *Ann. Rev. Fluid Mech.* **26**, 65–102.

YOUNGREN, G. K. & ACRIVOS, A. 1975 Stokes flow past a particle of arbitrary shape: a numerical method of solution. *J. Fluid Mech.* **69**, 377–403.

YOUNGREN, G. K. & ACRIVOS, A. 1976 On the shape of a gas bubble in a viscous extensional flow. *J. Fluid Mech.* **76**, 433–442.

ZICK, A. A. & HOMSY, G. M. 1982 Stokes flow through periodic arrays. *J. Fluid Mech.* **115**, 13–26.